lajss.org
Latin American Journal of Solids and Structures
www.lajss.org

Modeling of reinforced concrete beams subjected to four-point bending using tensor damage phase-field model.

Lucas Aragão de Assis[a] https://orcid.org/0009-0005-6081-3147, **Carlos Lamarca Carvalho Sousa Esteves**[a] https://orcid.org/0000-0003-0929-4431, **Eduardo Alexandre Rodrigues**[a] https://orcid.org/0000-0002-9416-8060, **José Luíz Boldrini**[a] https://orcid.org/0000-0003-4293-7611, **Marco Lúcio Bittencourt**[a*] https://orcid.org/0000-0002-5490-297X

[a]Department of Integrated Systems, School of Mechanical Engineering, University of Campinas, 13083-970, SP, Brazil. mlb@unicamp.br

* Corresponding author

Abstract

This study investigates the numerical modeling of failure mechanisms in reinforced concrete (RC) beams using the phase-field method, emphasizing its capability to simulate complex fracture behaviors under various loading conditions. The model incorporates a fourth-order degradation tensor to account for tensile, shear, and tensile-shear crack initiation and propagation. Six beam configurations from Marzec and Tejchman's experiments were modeled, varying dimensions, reinforcement ratios, and spans. The numerical results, obtained through finite element analyses, were compared with experimental data, revealing the model's accuracy in capturing crack patterns, failure mechanisms, and load-displacement responses. Key findings include the transition of failure modes from flexural to shear-dominated as beam slenderness decreases, consistent with experimental observations. Despite some discrepancies in peak load predictions, the phase-field model showed its potential for robust analysis of RC beam behavior, offering insights into fracture evolution and structural performance.

Keywords

Reinforced concrete beams, Phase-field method, Degradation tensor, Flexural-shear failure

Graphical Abstract

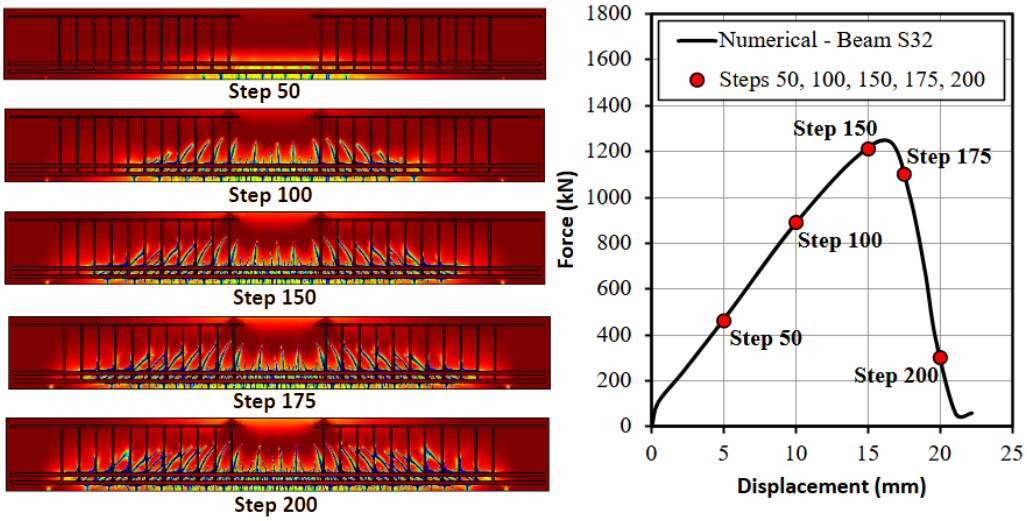

1 INTRODUCTION

Reinforced concrete (RC) beams are fundamental structural elements in modern construction, widely employed due to their cost-efficiency, ease of fabrication, and impressive compressive strength. The combination of brittle concrete and ductile steel reinforcement results in a composite material capable of withstanding both compressive and tensile loads, leveraging the strengths of each constituent material (Park and Paulay, 1991, Syal and Goel 2008, Guo 2014). Despite these advantages, the complex interplay between materials and the nonlinear fracture behavior of concrete pose significant challenges in accurately predicting the different failure mechanisms of RC beams under various loading conditions.

According to Zhu et al. (2007), and Xu et al. (2019) and Naderpour et al. (2021), there are three primary modes of failure in RC beams due to tensile and shear stresses: (i) flexural failure, where the beam's degradation is driven by bending after the yielding of longitudinal reinforcements (predominantly tensile stresses); (ii) shear failure where the beam's degradation is governed by shear stresses before the yielding of longitudinal reinforcements and (iii) flexural-shear failure, which results from a combination of tensile and shear stresses, where failure occurs after the yielding of longitudinal reinforcements but is primarily influenced by shear forces. Furthermore, Bažant and Planas (2019) highlight that variation in beam length or reinforcement ratio significantly affects the observed failure modes in RC beams. For instance, beams with shorter length, in general, primarily exhibited flexural-shear failure. Shear stresses play a dominant role in crack propagation, identified by the appearance of pronounced diagonal cracks surpassing vertical ones. For the other side, beams with the greatest slenderness, the flexural failure mode is predominant, in which vertical cracks along the beam's length are observed as indicated by others authors (Walraven and Lehwalter 1994, Belgin and Şener, 2008).

Due to the complex failure mechanism of RC beams (and other composite materials), numerical simulations have become indispensable tools for understanding their behavior, offering a cost-effective alternative to experimental testing. Finite element analysis (FEA) is a cornerstone of numerical modeling, allowing for detailed simulation of material behavior and structural response. In this context, continuous and discrete models have been proposed, with their advantages and limitations. Based either on the embedded discontinuity approach or on the mesh fragmentation technique, the works proposed by Oliver et al. (2008), Manzoli et al. (2014) and dos Santos et al. (2025) are examples of continuous models capable of efficiently representing the complex process of initiation and propagation of multiple fractures in RC beams subjected to bending, reproducing complex failure modes that are largely dependent on important factors, such as the slenderness of the beams and the longitudinal and transversal reinforcement ratios. On the other hand, the lattice particle model developed by Alnaggar et al. (2019) is an example of efficient discrete approach to simulate failure phenomena in RC beams.

Formulated within the framework of the continuum approach, the phase-field method, in particular, has gained prominence for its ability to model fractures as diffuse zones within the material, eliminating the need for explicit crack tracking and enabling automatic representation of complex crack patterns. Rooted in Griffith's energy theory, this method balances elastic strain energy and crack surface energy (Molnár, G. and Gravouil 2017, Wu 2018, Feng and Wu 2018, Wu et al. 2020, Ahmed et al. 2023), making it well-suited for studying the failure of RC beams under bending, shear, and combined loading conditions. The method has been effectively applied to modeling the crack propagation in conventional concrete (Feng and Wu 2018, Wang et al. 2021, Lateef et al. 2022, Ahmed et al. 2023), ultra-high and high performance concrete (Zhao et al. 2022, Schröder et al. 2022), asphaltic concrete (Ahmed and Khan 2022) and composite materials, such as reinforced concrete (Ding et al. 2024), reinforced ultra-high performance concrete at low cycle fatigue (Pise et al. 2023) and fiber-reinforced concrete (Espadas-Escalante et al. 2019, Sadighi et al. 2023).

In this work, a comprehensive study on the numerical modeling of RC beams is presented where a phase-field model is applied to simulate the complex flexural-shear failure mechanism. A fourth-order degradation tensor based phase field model developed in (Petrini et al. 2021, Petrini et al. 2023, Petrini et al. 2023) is used to account for the tensile, shear or tensile-shear cracks initiation and propagation in the concrete. For the sake of simplicity, a linear elastic behavior is assumed for the concrete in compression. Furthermore, a perfect bond is adopted to represent the interaction between the steel bars and the concrete. The six beam configurations experimentally tested by Marzec and Tejchman (2022) were simulated, varying the dimensions, reinforcement ratios, and spans. The numerical results are compared with experimental data, highlighting the accuracy and versatility of the proposed model in capturing crack patterns, failure mechanisms, and structural responses of RC beams under flexural loading conditions.

2 BRIEF DESCRIPTION OF THE PHASE-FIELD FORMULATION

This study employs a phase-field model for brittle fracture under small strain assumptions and isothermal conditions. The governing differential equations are given as follows (Petrini et al. 2021, Petrini et al. 2023, Petrini et al. 2023):

$$\begin{cases} \rho\ddot{\boldsymbol{u}} = div\boldsymbol{T} + \boldsymbol{f} \\ \boldsymbol{T} = \rho\psi_{\boldsymbol{E}} - \rho sym(\psi_{\nabla\mathbb{G}} :: \nabla\mathbb{G}) + \hat{b}\boldsymbol{D}. \\ \dot{\mathbb{G}} = -\hat{F}\left[\frac{\rho_0}{\theta}\psi_{\mathbb{G}} - div\left(\frac{\rho_0}{\theta}\psi_{\nabla\mathbb{G}}\right)\right] \end{cases} \tag{1}$$

where ρ is the material density, $\boldsymbol{u}$ and $\ddot{\boldsymbol{u}}$ are the displacement and acceleration vector fields, respectively, $\boldsymbol{T}$ is the stress tensor field, f is the body force vector field, $\boldsymbol{E}$ is the strain tensor field, $\mathbb{G}$ is the fourth-order degradation tensor, $\boldsymbol{D}$ is the symmetric velocity gradient, $\hat{b}$ and $\hat{F}$ are positive constants.

The constitutive energy relations are defined as

$$\begin{cases} \rho\psi = \mathfrak{E} + \mathcal{J}, \\ 2\mathfrak{E} = \boldsymbol{E} : \mathbb{G} : \mathbb{C}^0 : \mathbb{G} : \boldsymbol{E}, \\ \mathcal{J} = \frac{g_c}{2l}|\mathbb{I}_s - \mathbb{G}|^2 + \frac{g_c l}{2}|\nabla\mathbb{G}|^2, \end{cases} \tag{2}$$

where $\mathfrak{E}$ and $\mathcal{J}$ represent the elastic energy and the surface fracture energy, respectively. $\mathbb{C}^0$ is the virgin fourth-order elasticity tensor. Material-specific parameters include the characteristic fracture length (l) and the Griffith's surface energy (g_c). $\mathbb{I}_s$ is the symmetric fourth-order identity tensor given by

$$(\mathbb{I}_s)_{ijkl} = (\delta_{ik}\delta_{jl} + \delta_{il}\delta_{jk}). \tag{3}$$

The problem is split into two coupled subproblems: one for the displacement field and another one for the degradation field. Weak forms are developed for each subproblem and approximated using linear finite elements. The finite element operators, for the displacement field subproblem are

$$\begin{aligned} &\boldsymbol{M}_u^e = \rho\int_{\Omega_e}\boldsymbol{N}_u{}^T\boldsymbol{N}_u d\Omega_e, \boldsymbol{K}_u^e = \int_{\Omega_e}\boldsymbol{B}_u{}^T[\mathbb{G} : \mathbb{C}^0 : \mathbb{G}]\boldsymbol{B}_u d\Omega_e, \\ &\boldsymbol{K}_v^e = \hat{b}\int_{\Omega_e}\boldsymbol{B}_u{}^T\boldsymbol{B}_u d\Omega_e, \boldsymbol{w}_a^e = g_c l\int_{\Omega_e}\boldsymbol{B}_u{}^T[\nabla\mathbb{G} :: \nabla\mathbb{G}]d\Omega_e, \end{aligned} \tag{4}$$

which are assembled globally to yield the following approximate equation:

$$\boldsymbol{M}_u\hat{\ddot{\boldsymbol{u}}} + \boldsymbol{K}_v\hat{\dot{\boldsymbol{u}}} + \boldsymbol{K}_u\hat{\boldsymbol{u}} = \boldsymbol{w}_a. \tag{5}$$

Time integration is performed using the Newmark's implicit method, where the effective stiffness matrix at time t_{n+1} is given by

$$\boldsymbol{K}_{eff} = \boldsymbol{K}_u + a_0\boldsymbol{M}_u + a_1\boldsymbol{K}_v, \tag{6}$$

Similarly, the finite element operators for the degradation field subproblem are

$$\boldsymbol{Q}_g^e = \hat{F}\int_{\Omega_e} \boldsymbol{N}_g{}^T[\boldsymbol{E} \otimes \mathbb{C}^0 \otimes \boldsymbol{E}]\boldsymbol{N}_g d\Omega_e, \boldsymbol{K}_g^e = \int_{\Omega_e} \boldsymbol{B}_g{}^T \boldsymbol{B}_g d\Omega_e,$$
$$\boldsymbol{M}_g^e = \int_{\Omega_e} \boldsymbol{N}_g{}^T \boldsymbol{N}_g d\Omega_e, \boldsymbol{w}_b^e = \hat{F}\frac{g_c}{l}\kappa\int_{\Omega_e} \boldsymbol{N}_g{}^T\{\mathbb{I}_s\}d\Omega_e, \tag{7}$$

resulting in the global equation

$$\boldsymbol{M}_g\hat{\dot{\mathbb{G}}} + \hat{F}\boldsymbol{Q}_g\hat{\mathbb{G}} + \hat{F}g_c l\boldsymbol{K}_g\hat{\mathbb{G}} + \hat{F}\frac{g_c}{l}\kappa\boldsymbol{M}_g = \boldsymbol{w}_b. \tag{8}$$

Parameter κ is a bulk energy scaling factor to speed-up the fracture propagation.

For time-stepping, the backward Euler method is used, leading to

$$\left[\left(1 + \hat{F}\Delta t\frac{g_c}{l}k\right)\boldsymbol{M}_g + \hat{F}\Delta t\boldsymbol{Q}_g + \hat{F}\Delta t g_c l\boldsymbol{K}_g\right]\left\{\hat{\dot{\mathbb{G}}}_{n+1}\right\} = \boldsymbol{M}_g\left\{\hat{\mathbb{G}}_n\right\} + \Delta t\boldsymbol{w}_b, \tag{9}$$

in which $\hat{\dot{\mathbb{G}}}_{n+1}$ is defined by

$$\hat{\dot{\mathbb{G}}}_{n+1} = \frac{1}{\Delta t}\left(\hat{\mathbb{G}}_{n+1} - \hat{\mathbb{G}}_n\right). \tag{10}$$

Finally, degradation irreversibility is guaranteed by solving the eigenvalue problem for the degraded elasticity tensor $\mathbb{C} = \mathbb{G} : \mathbb{C}^0 : \mathbb{G}$. Using the geometric average of eigenvalues, $\zeta = \sqrt[k]{\prod_{i=1}^{k}\lambda_i}$, which k is of the same order of $\mathbb{C}$, the scalar damage variable $\zeta_r = \zeta^{(n)}/\zeta^{(0)}$ is monitored, with degradation constrained to $\dot{\zeta}_r \leq 0$.

It is important to mention that only the most relevant equations of the formulation are presented and further details can be found in Petrini et al. (2021) and Petrini et al. (2023).

3 RESULTS

The six beams experimentally tested by Marzec and Tejchman (2022) are numerically simulated, using the phase-field model presented previously. In the experiments, two series called series '3' and series '4' were considered either scaled along beam's height or length. In the case of beam series '3', the shear span was varied (i.e., α = 0.54, 1.08 and 2.16 m), keeping the effective depth and thickness constants ($D = 0.36m$ and $t = 0.25m$) and resulting in the shear span parameters, i.e., $n_a = a/D$, 1.5, $3.0$and 6.0, as illustrated in Figure 1. The same longitudinal and shear steel reinforcement ratios of $p_l = 4.3\%$ and $p_s = 4.0\%$ were used for all the beams of series '3'. For beams of series '4', the shear span is kept constant, $a = 1.08m$, varying effective depth $D =$

0.220,0.430,0.720, resulting in approximate values of the shear span parameter of $n_a = 1.5,2.5,5.0$, as shown in Figure 2. The respectively longitudinal reinforcement ratios of $p_l = 3.5\%$, $p_l = 3.5\%$ and $p_l = 4.3$ were assumed, maintaining the same shear reinforcement ratio of $p_s = 4.3\%$ for the stirrups. As highlighted by the authors of the experiment (Marzec and Tejchman 2022), all beams were over-reinforced to avoid steel yield failure. For the sake of simplicity, the six simulated beams are labeled as S31, S32 and S33 for the series '3' and S41, S42 and S43 for the series '4', respectively.

Four-node quadrilateral finite elements were used to discretize the beams (concrete and reinforcement domains), as illustrated in Figure 3. The total number of finite elements for each beam are as follows: $S31 = 305{,}829$; $S32 = 338{,}802$; $S33 = 450{,}783$; $S41 = 314{,}955$; $S42 = 342{,}314$ and $S43 = 440{,}449$. The mesh refinement for the different beams was selected to ensure a uniform size of the finite elements in all cases. Thus, the element size was determined based on the first analyses, where the results indicated that the level of mesh refinement was sufficient to achieve a good convergence of the qualitative and quantitative responses.

The elastic and phase-field parameters assumed for the concrete are Young's modulus of $34.0GPa$, Poisson's ratio of 0.2, material density of $2400kg/m^3$, Griffith energy of $100J/m^2$and $k = 0.00003$ and characteristic fracture length of $1.0x10^{-6}$. It is important to mention that the k and Griffith parameters are calibrated through reverse analysis to obtain the same tensile strengths of concrete, as obtained experimentally by Marzec and Tejchman (2022). For the steel reinforcements the same phase-field approach enhanced with a fourth-order degradation tensor was used. The properties are: Young's modulus of $210.0GPa$, Poisson's ratio of 0.24 and material density of $7300kg/m^3$. The Griffith energy of $2000J/m^2$ and $k = 0.008$ were obtained also from axial tensile tests for a single sample to obtain the yield stress of 580MPa, as given by Marzec and Tejchman (2022). It is important to note that the beams were over-reinforced by the authors of the experiments to prevent failure due to steel yielding.

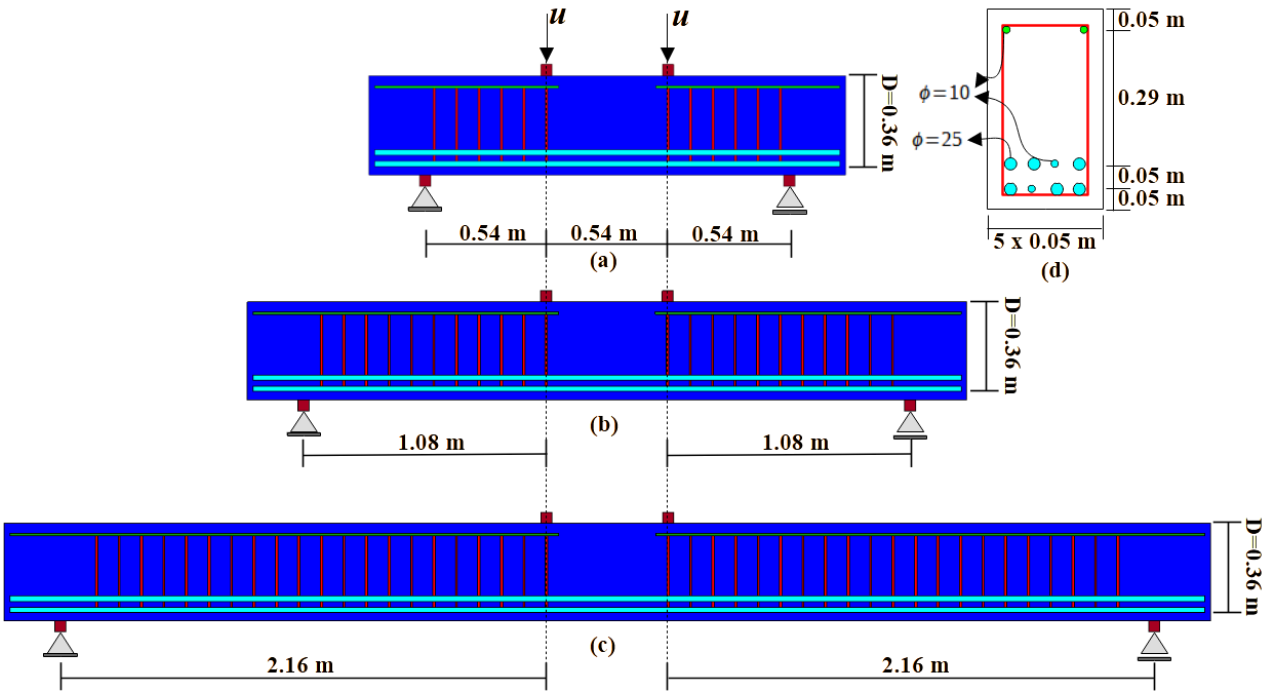

Figure 1 *Geometry of the reinforced concrete beams of series '3' with shear span parameters of : (a)* $n_a = 1.5$ *,* $n_a = 3.0$ *and* $n_a = 6.0$.

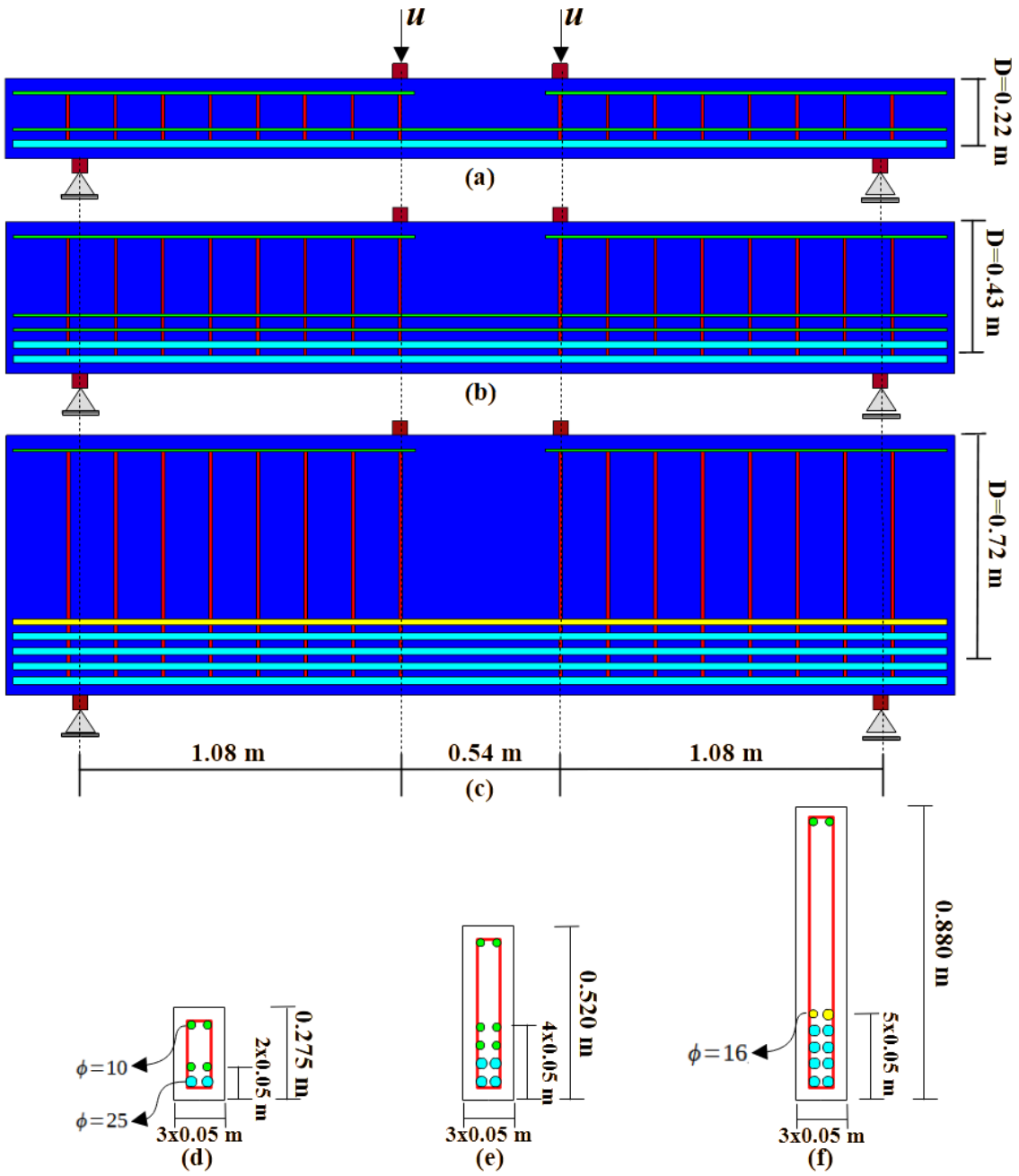

Figure 2 *Geometry of the reinforced concrete beams of series '4' with shear span parameters and corresponding cross-sections of: (a and d)* $n_a = 1.5$ *, (b and e)* $n_a = 2.5$*, (c and f)* $n_a = 5.0$*,*

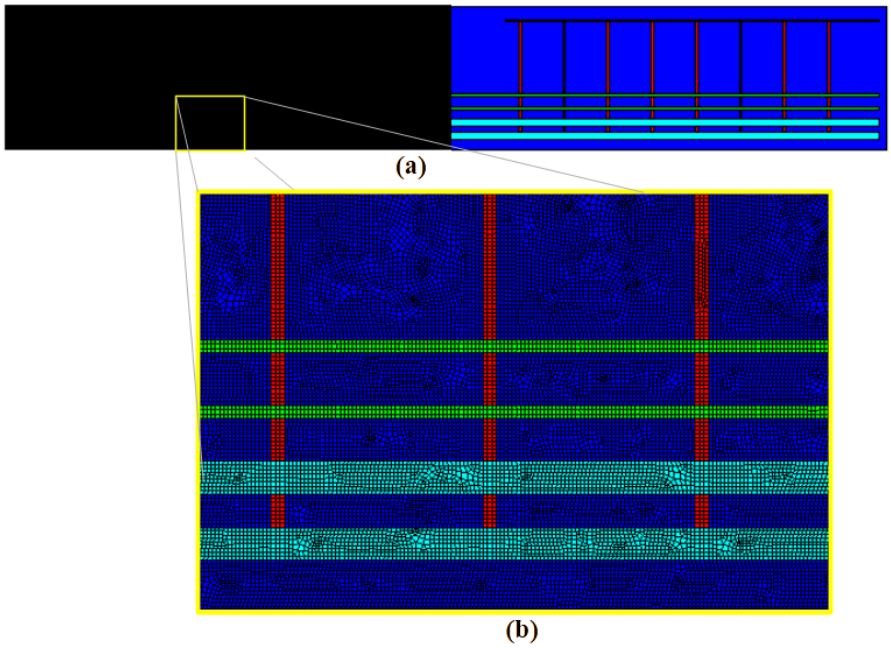

Figure 3 *FE mesh adopted for the beam S42: (a) illustration of discretization/geometry and (b) zoom showing mesh details.*

For the developed 2D numerical analyses, a plane stress state is assumed and incremental displacement is applied with a rate of $\boldsymbol{u} = 0.0001 m/s$ per time step.

Figure 4 illustrates the distribution of the scalar damage variable ζ for the beams of series '3'. It is possible to observe the transition from diagonal shear cracks to tensile cracks due to bending. For the shortest beam, flexural cracks in the tensile region of the beam can be observed. However, failure occurs due to the coalescence of diagonal shear fractures, as illustrated in Figure 4(a). In the case of the intermediate beam, both tensile failures due to bending and shear fracture are equally predominant (see Figure 4(b)). For the slender beam, tensile cracks are predominant, leading to the failure of the structural element, as shown in Figure 4(c). In Figure 5, the reaction force *versus* the imposed displacement is plotted and compared against the experimental results obtained by Marzec and Tejchman (2022). In general, the numerical curves reproduced the experimental responses well. For the shortest beam, the peak load overestimated the experimental result, indicating that neglected compression failure in this work may be important, since the concrete behavior under compression is assumed to be linear-elastic. In the case of beam S33, failure occurred abruptly at an applied load of approximately 586.0 kN which corresponds to the imposed displacement of about 40.4 mm for the peak load. Due to the sudden nature of the failure, it was not possible to capture the post-peak response for this specimen.

Figure 6 presents the historical evolution of the crack pattern for different steps for the intermediate beam S32. In the initial loading stage, only tensile cracks due to bending can be observed (see Figure 6(a)). As illustrated in Figure 6(b, c and d), for the steps 100, 150 and 175, these cracks continue to propagate with the progressive increase in loading, and the formation of tensile and diagonal shear cracks patterns, resulting in the beam's failure (see Figure 6(e)). In Figure 7, the reaction force is plotted against the imposed displacement, where the 50th, 100th, 150th, 175th and 200th load steps are indicated, presenting a correspondence with the qualitative results of Figure 6(a-e).

On the other hand, the simulated beams of the series '4' present an opposite transition to the series '3' beams, i.e., predominant tensile cracks to dominated diagonal shear cracks patterns are observed as the effective height of the beam increases, as illustrated in Figure 8. For beam S41, tensile cracks due to bending are predominant and lead to its failure (see Figure 8(a)). In the case of the intermediate beam S42, both tensile and shear cracks are important, contributing equally to beam failure (see Figure 8(b)). As presented in Figure 8(c) for the less slender beam S43, diagonal shear cracks are dominant and produce the collapse of the reinforced beam.

In Figure 9, the numerical curves of reaction force *versus* imposed displacement obtained are compared with the experimental responses, showing good agreement, except for beam S43, which again overestimated the experimental peak load. The evolution of the damage field for some loading steps obtained for beam S42 is shown

in Figure 10, where the process of initiation, propagation and coalescence of fractures can be observed throughout the analysis. The corresponding reaction force *versus* imposed displacement for these steps are indicated in the numerical curve plotted in Figure 11.

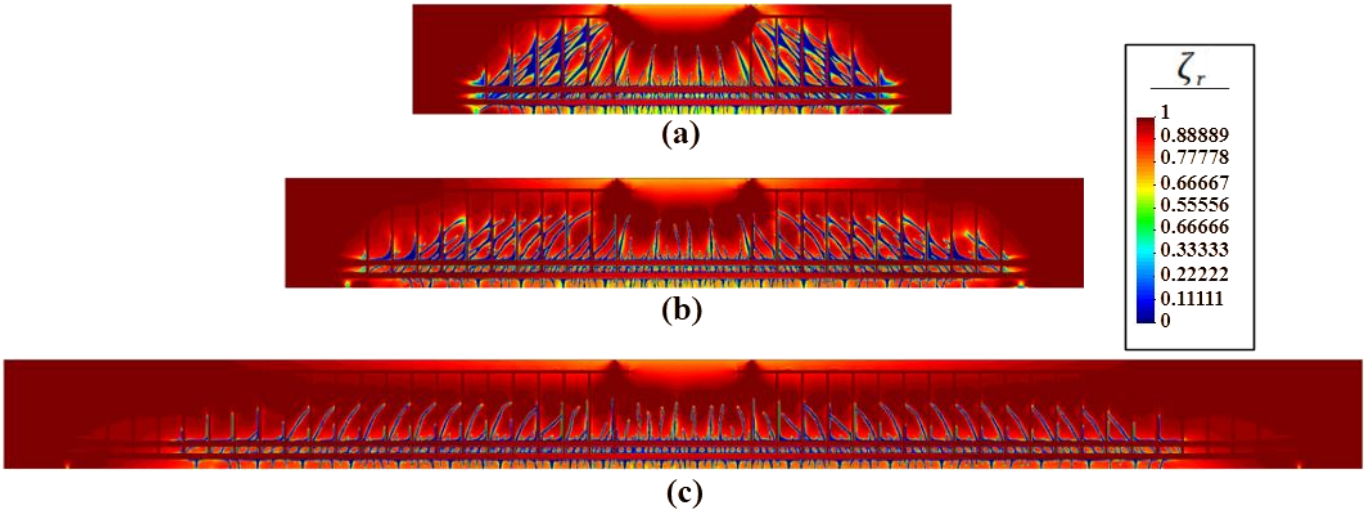

Figure 4 Damage fields for the reinforced beams of series '3': (a) S31, (b) S32 and (c) S33.

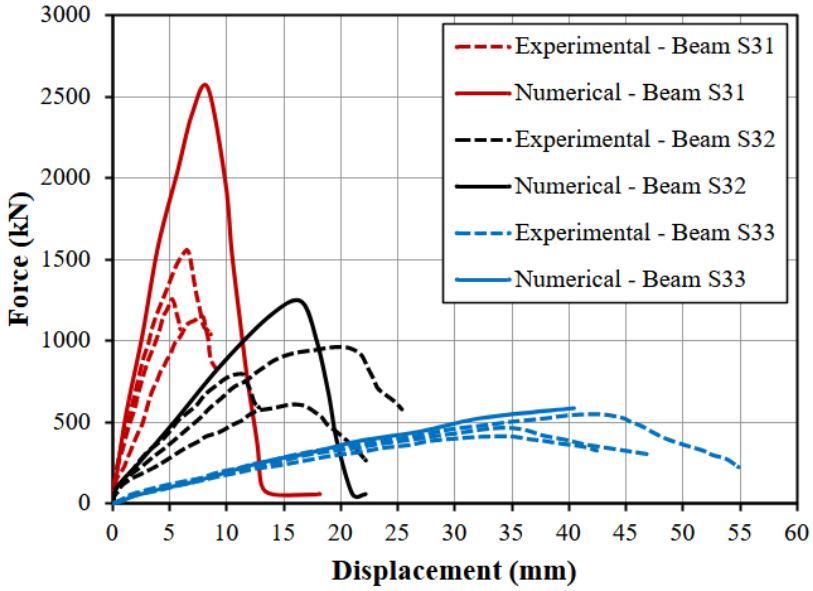

Figure 5 Reaction force against imposed displacement curves for beams of series '3'.

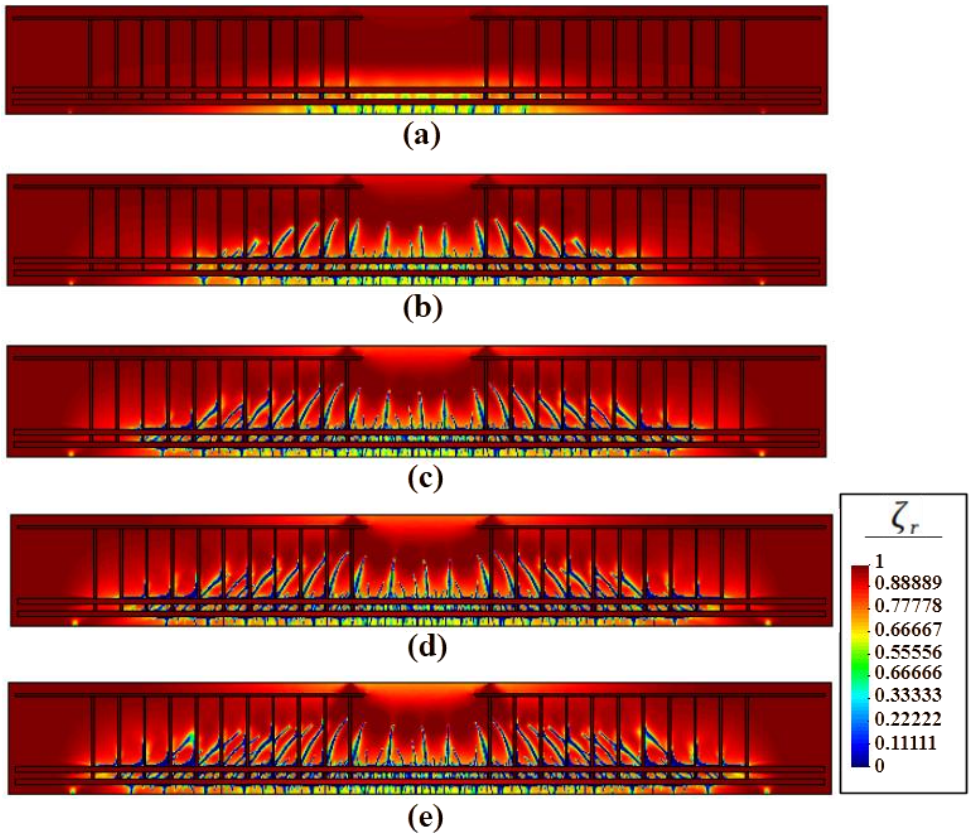

Figure 6 Damage fields for the beam S32 of series '3' for different loading steps: (a) 50, (b) 100, (c) 150, (d) 175 and (e) 200.

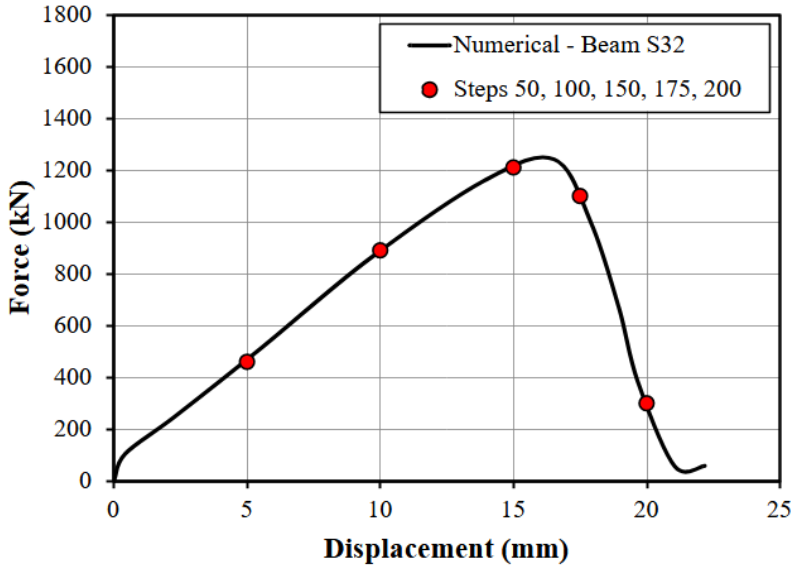

Figure 7 Reaction force against imposed displacement curve for beam S32 of series '3', indicating the 50th, 100th, 150th, 175th and 200th load steps.

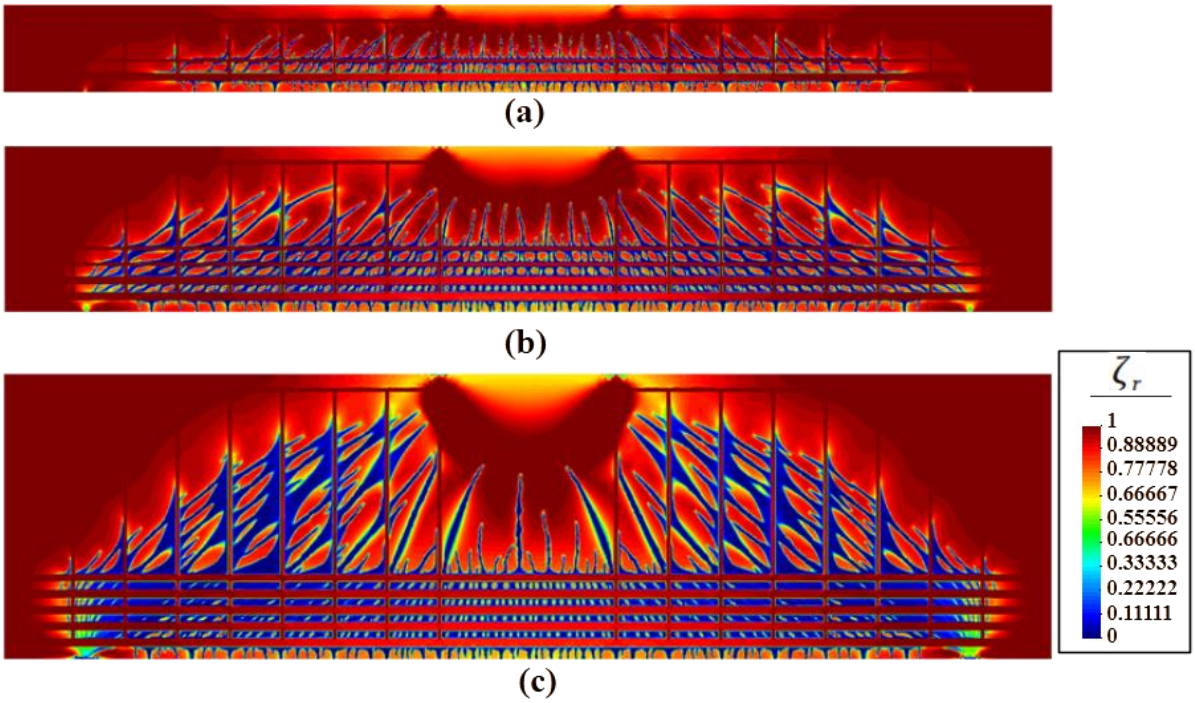

Figure 8 Damage fields for the reinforced beams of series '4': (a) S41, (b) S42 and (c) S43.

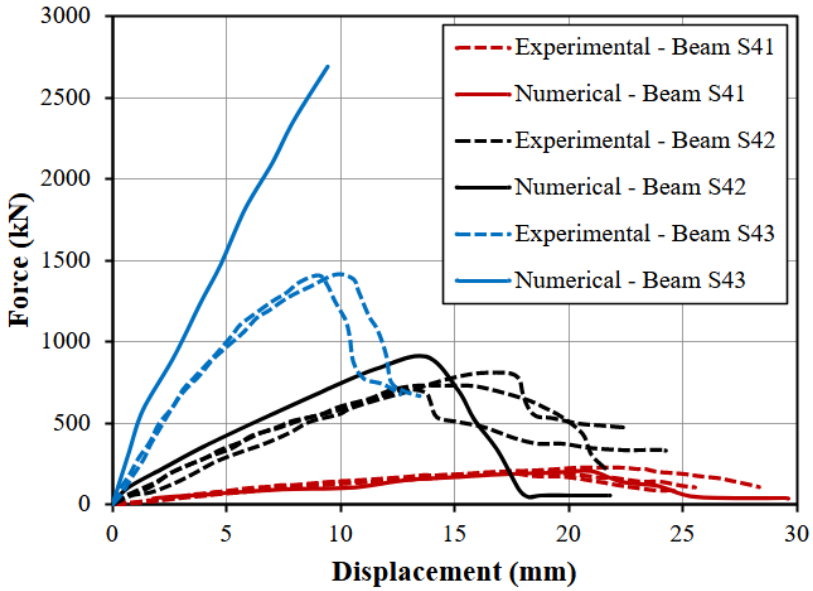

Figure 9 Reaction force against imposed displacement curves for beams of series '4'.

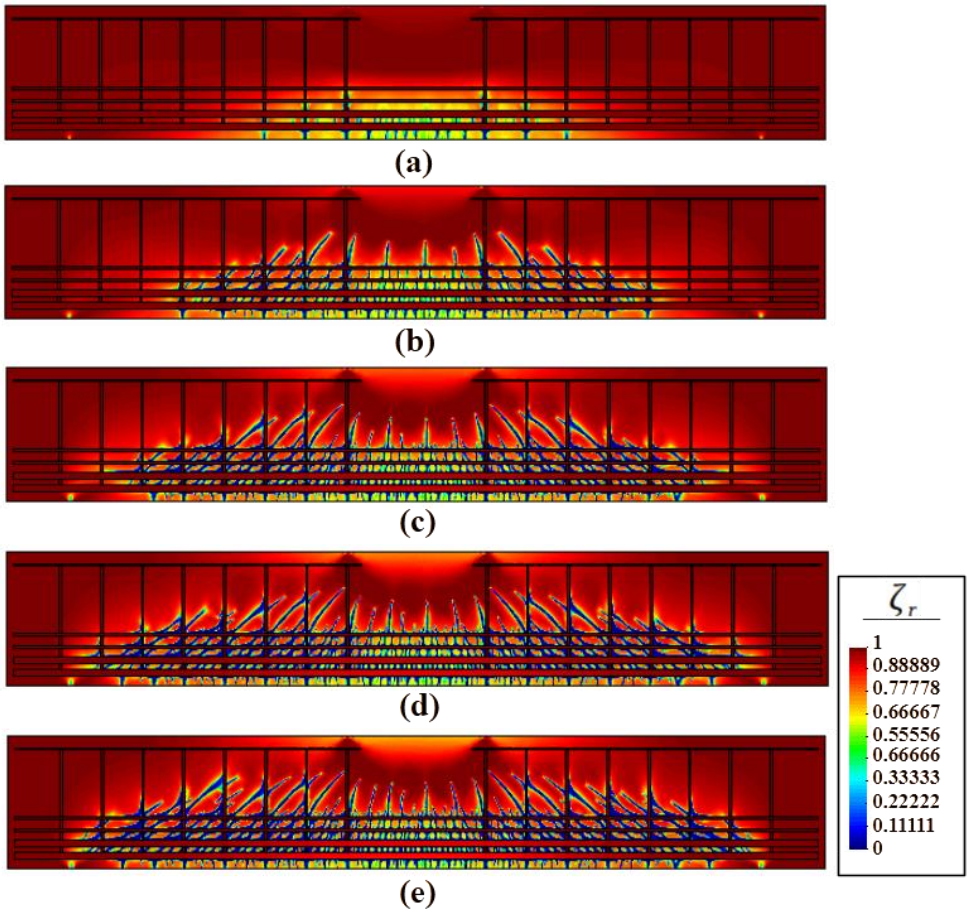

Figure 10 Damage fields for the beam S42 of series '4' for different loading steps: (a) 50, (b) 100, (c) 150, (d) 175 and (e) 200.

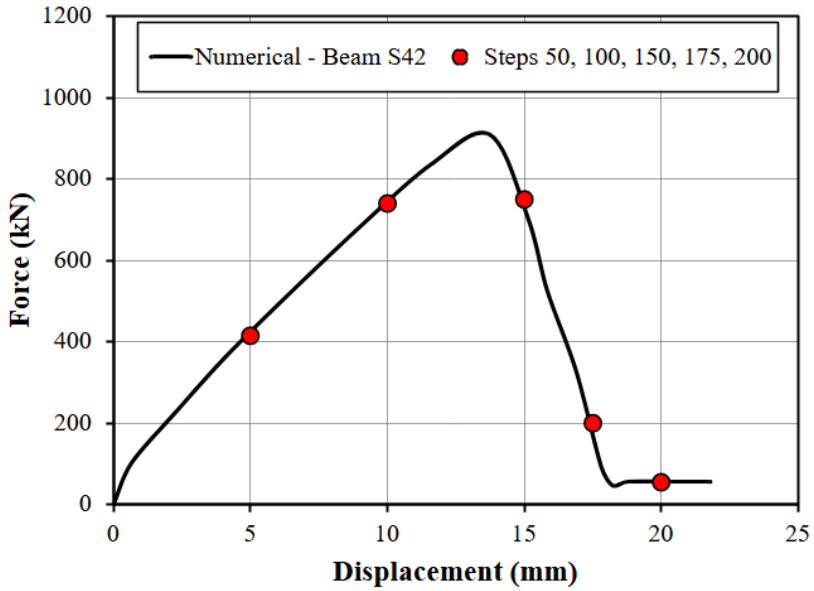

Figure 11 Reaction force against imposed displacement curve for beam S42 of series '4', indicating the 50th, 100th, 150th, 175th and 200th load steps.

4 CONCLUSIONS

This study highlighted the applicability and accuracy of a phase-field approach in modeling the complex failure mechanisms of reinforced concrete (RC) beams. By using a fourth-order degradation tensor, the approach effectively captured the initiation and propagation of tensile, shear, and combined tensile-shear cracks, providing a nuanced understanding of the fracture behavior under diverse loading conditions.

The results demonstrated that the model reliably reproduces experimental observations, including the progression of crack patterns, structural responses, and failure modes. Specifically, the numerical simulations captured the transition from flexural failure in slender beams to shear-dominated failure in shorter beams, aligning well with established experimental trends. The simulation outcomes also illustrated how variations in the beam geometry, such as span-to-depth ratios and reinforcement configurations, significantly influence crack evolution and structural failure.

While the phase-field method showed good agreement with experimental data, some discrepancies were also observed, particularly in the peak load predictions for beams dominated by shear failure. The deviations suggest that the model could benefit from further refinements to account for concrete's behavior under compressive stresses, which is currently modeled as linear-elastic in this study. Addressing this limitation may improve the accuracy of the load-bearing capacity predictions, especially for shear-dominated configurations.

Overall, the phase-field method showed to be a robust and versatile tool for investigating RC beam behavior, offering a detailed insight into structural performance and failure mechanisms. This approach not only provides a cost-effective alternative to experimental testing but also paves the way for more advanced modeling of complex fracture processes in reinforced concrete structures. Future research could explore enhancements to the material model, including the integration of nonlinear compressive behavior, to further extend the method's applicability to broader structural scenarios.

Acknowledgments

The authors wish to acknowledge the financial support of the National Council for Scientific and Technological Development - CNPq, Brazil (Processes 140214/2022-4 and 307488/2022-5), Coordination for the Improvement of Higher Education Personnel (CAPES), Brazil and São Paulo Research Foundation - FAPESP, Brazil (Processes: 2023/03047-0 and 2023/13651-1).

Author's Contributions: Conceptualization, JL Boldrini and ML Bittencourt; Methodology, JL Boldrini and ML Bittencourt; Investigation, JL Boldrini, ML Bittencourt, CLCS Esteves, EA Rodrigues and LA de Assis; Writing - original draft, JL Boldrini, ML Bittencourt, CLCS Esteves, EA Rodrigues; Writing - review & editing, JL Boldrini, ML Bittencourt, CLCS Esteves, EA Rodrigues; Funding acquisition, ML Bittencourt; Resources, JL Boldrini and ML Bittencourt; Supervision, JL Boldrini and ML Bittencourt.

Editor: Eduardo Alberto Fancello and Paulo de Tarso Mendonça

References

Ahmed, A. and Khan, R. (2022). A phase field model for damage in asphalt concrete. International Journal of Pavement Engineering 23(12): 4320-4332.

Ahmed, A., Liu, Y., Tafsirojjaman, T., Ahmad, A. and Iqbal, M. (2023). Phase field model for mixed mode fracture in concrete. Engineering Fracture Mechanics 289: 109439.

Alnaggar, M., Pelessone, D. Cusatis, G. (2019). Lattice discrete particle modeling of reinforced concrete flexural behavior. Journal of Structural Engineering 145(1): 04018231.

Bazant, Z. P. and Planas, J. (2019). Fracture and size effect in concrete and other quasibrittle materials. Routledge.

Belgin, Ç. M. and Şener, S. (2008). Size effect on failure of overreinforced concrete beams. Engineering Fracture Mechanics 75(8): 2308-2319.

Ding, J., Wang, X., Liu, S., Lei, M., Liang, M. and Wu, Z. (2024). Phase-field anisotropic damage with bond-slip model for reinforced concrete beam under the service load. Engineering Fracture Mechanics 307: 110317.

dos Santos, A. F. V., Gimenes, M., Rodrigues, E. A., Cleto, P. R. and Manzoli, O. L. (2025). Modeling different modes of failure in reinforced concrete beams combining tensile and shear-frictional damage models and bond–slip coupling for non-matching reinforcement and fragmented concrete meshes. Engineering Structures 323: 119265.

Espadas-Escalante, J. J., van Dijk, N. P., & Isaksson, P. (2019). A phase-field model for strength and fracture analyses of fiber-reinforced composites. Composites Science and Technology, 174, 58-67.

Feng, D. C. and Wu, J. Y. (2018). Phase-field regularized cohesive zone model (CZM) and size effect of concrete. Engineering Fracture Mechanics 197: 66-79.

Guo, Z. (2014). Principles of reinforced concrete. Butterworth-Heinemann.

Lateef, H. A., Laftah, R. M. and Jasim, N. A. (2022). Investigation of crack propagation in plain concrete using Phase-field model. Materials Today: Proceedings 57: 375-382.

Manzoli, O. L., Maedo, M. A., Rodrigues, E. A. and Bittencourt, T. (2014). Modeling of multiple cracks in reinforced concrete members using solid finite elements with high aspect ratio. Computational modelling of concrete structures, 1, 383-92.

Marzec, I. and Tejchman, J. (2022). Experimental and numerical investigations on RC beams with stirrups scaled along height or length. Engineering Structures 252: 113621.

Molnár, G. and Gravouil, A. (2017). 2D and 3D Abaqus implementation of a robust staggered phase-field solution for modeling brittle fracture. Finite Elements in Analysis and Design 130: 27-38.

Naderpour, H., Mirrashid, M. and Parsa, P. (2021). Failure mode prediction of reinforced concrete columns using machine learning methods. Engineering Structures 248: 113-263.

Oliver, J., Linero, D. L., Huespe, A. E. and Manzoli, O. L. (2008). Two-dimensional modeling of material failure in reinforced concrete by means of a continuum strong discontinuity approach. Computer Methods in Applied Mechanics and Engineering 197(5): 332-348.

Petrini, A. L. E. R., Boldrini, J. L. and Bittencourt, M. L. (2021). A thermodynamically consistent phase field framework for anisotropic damage propagation. Latin American Journal of Solids and Structures 18(1): e314.

Petrini, A. L. E. R., Esteves, C. L. C. S., Boldrini, J. L. and Bittencourt, M. L. (2023). A fourth-order degradation tensor for an anisotropic damage phase-field model. Forces in Mechanics 12: 100224.

Petrini, A. L. E. R., Esteves, C. L. C. S., Boldrini, J. L. and Bittencourt, M. L. (2023). Brittle Anisotropy based on a Tensor Damage Phase Field Model. Latin American Journal of Solids and Structures 20(6): e507.

Pise, M., Gebuhr, G., Brands, D., Schröder, J. and Anders, S. (2023). Phase-field modeling for failure behavior of reinforced ultra-high performance concrete at low cycle fatigue. PAMM 23(3): e202300233.

Park, R. and Paulay, T. (1991). Reinforced concrete structures. John Wiley & Sons.

Sadighi, A., Maghami, E., Khaneghahi, M. H., Kamireddi, D., Rahmaninezhad, S. A., Farnam, Y. A., ... and Najafi, A. R. (2023). Fracture analysis of multifunctional fiber-reinforced concrete using phase-field method. International Journal of Solids and Structures 283: 112493.

Schröder, J., Pise, M., Brands, D., Gebuhr, G. and Anders, S. (2022). Phase-field modeling of fracture in high performance concrete during low-cycle fatigue: Numerical calibration and experimental validation. Computer methods in applied mechanics and engineering 398: 115181.

Syal, I. C. and Goel, A. K. (2008). Reinforced Concrete Structure. S. Chand Publishing.

Walravena, J. and Lehwalter, N. (1994). Size effects in short beams loaded in shear. Structural Journal 91(5): 585-593.

Wang, J., Guo, X. and Zhang, N. (2021). Study of the progressive failure of concrete by phase field modeling and experiments. International Journal of Damage Mechanics 30(9): 1377-1399.

Wu, J. Y. (2018). A geometrically regularized gradient-damage model with energetic equivalence. Computer Methods in Applied Mechanics and Engineering 328: 612-637.

Wu, J. Y., Nguyen, V. P., Nguyen, C. T., Sutula, D., Sinaie, S. and Bordas, S. P. (2020). Phase-field modeling of fracture. Advances in applied mechanics 53: 1-183.

Xu, T. and Li, J. (2019). Experimental investigations of failure modes of reinforced concrete beams without web reinforcement. Engineering Structures 185: 47-57.

Zhao, B., Xu, Y., Peng, H., Pan, J., Li, T., Zhang, Z. and Peng, X. (2022). Experiment and phase-field simulation of uniaxial compression of ultra-high-performance concrete with coarse aggregate. Advances in Structural Engineering 25(10): 2121-2136.

Zhu, L., Elwood, K. J. and Haukaas, T. (2007). Classification and seismic safety evaluation of existing reinforced concrete columns. Journal of Structural Engineering 133(9): 1316-1330.